Remotely sensed river surface features compared with modeling and in situ measurements

William J. Plant,[1] Ruth Branch,[1] Gene Chatham,[1] C. Chris Chickadel,[1] Ken Hayes,[1] Bronwyn Hayworth,[2,3] Alexander Horner-Devine,[2] Andrew Jessup,[1] Derek A. Fong,[4] Oliver B. Fringer,[4] Sarah N. Giddings,[4] Stephen Monismith,[4] and Bing Wang[4]

[1]   Images of river surface features that reflect the bathymetry and flow in the river have been obtained using remote sensing at microwave, visible, and infrared frequencies. The experiments were conducted at Jetty Island near the mouth of the Snohomish River at Everett, Washington, where complex tidal flow occurs over a varied bathymetry, which was measured as part of these experiments. An X band (9.36 GHz) Doppler radar was operated from the river bank and produced images of normalized radar cross sections and radial surface velocities every 20 min over many tidal cycles. The visible and infrared instruments were flown in an airplane. All of these techniques showed surface evidence of frontal features, flow over a sill, and flow conditioned by a deep hole. These features were modeled numerically, and the model results correspond well to the remote observations. In situ measurements made near the hole showed that changes in measured velocities correlate well with the occurrence of the features in the images. In addition to tidal phase, the occurrence of these features in the imagery depends on tidal range. The surface roughness observed in the imagery appears to be generated by the bathymetry and flow themselves rather than by the modulation of wind waves.

1. Introduction

[2]   Microwave radars are increasingly being used to image surface roughness and to measure surface velocities in rivers. Standard synthetic aperture radars have been used to image river roughness and width, while interferometric synthetic aperture radars have been shown to yield measurements of surface velocity in rivers with high spatial resolution from both aircraft and spacecraft [*Brakenridge et al.*, 1994; *Horritt et al.*, 2001; *Bjerklie et al.*, 2005; *Romeiser et al.*, 2007]. Coherent real aperture radars have also been used to image surface roughness and velocities from aircraft [*Plant et al.*, 2005a]. When used from helicopters, riverbanks, bridges, or cableways, coherent microwave systems have been shown to provide accurate measurements of horizontal profiles of surface velocity across rivers [*Yamaguchi and Niizato*, 1994; *Melcher et al.*, 2002; *Plant et al.*, 2005a, 2005b; *Costa et al.*, 2006]. Beds of rivers have been mapped using lower-frequency ground-penetrating radars but so far have only been demonstrated for nadir operation from bridges, helicopters, and cableways [*Spicer et al.*, 1997; *Costa et al.*, 2000; *Melcher et al.*, 2002; *Costa et al.*, 2006]. For rivers in which the bed is relatively stable, both microwave and UHF radar measurements of surface velocity profiles can provide the discharge of rivers as accurately as the more standard method that relies on surface elevation [*Costa et al.*, 2006].

[3]   To date, ground-penetrating radars have not demonstrated the capability of imaging river beds from off-nadir angles or from high altitudes. In any case, these systems tend to be large and awkward to operate from aircraft. Visible and infrared imagery have also not successfully determined bed characteristics of rivers to date. Thus, the challenge still remains to determine features of river beds from images of the surface produced by smaller microwave systems, whose radiation does not significantly penetrate the water, or by visible or infrared techniques. In this paper we demonstrate that bottom features in rivers modify the surface roughness, velocity, and temperature of the river. We use in situ measurements to determine the bathymetry, currents, and density in a highly variable region near the mouth of a river. We show that the currents and bathymetry produce distinctive signatures in microwave, visible, and infrared images of surface roughness, velocity, and temperature, which correspond to flow features produced by a numerical model and measured by an acoustic Doppler

[1]Applied Physics Laboratory, University of Washington, Seattle, Washington, USA.
[2]Department of Civil and Environmental Engineering, University of Washington, Seattle, Washington, USA.
[3]Now at U. S. Environmental Protection Agency, Denver, Colorado, USA.
[4]Department of Civil and Environmental Engineering, Stanford University, Stanford, California, USA.
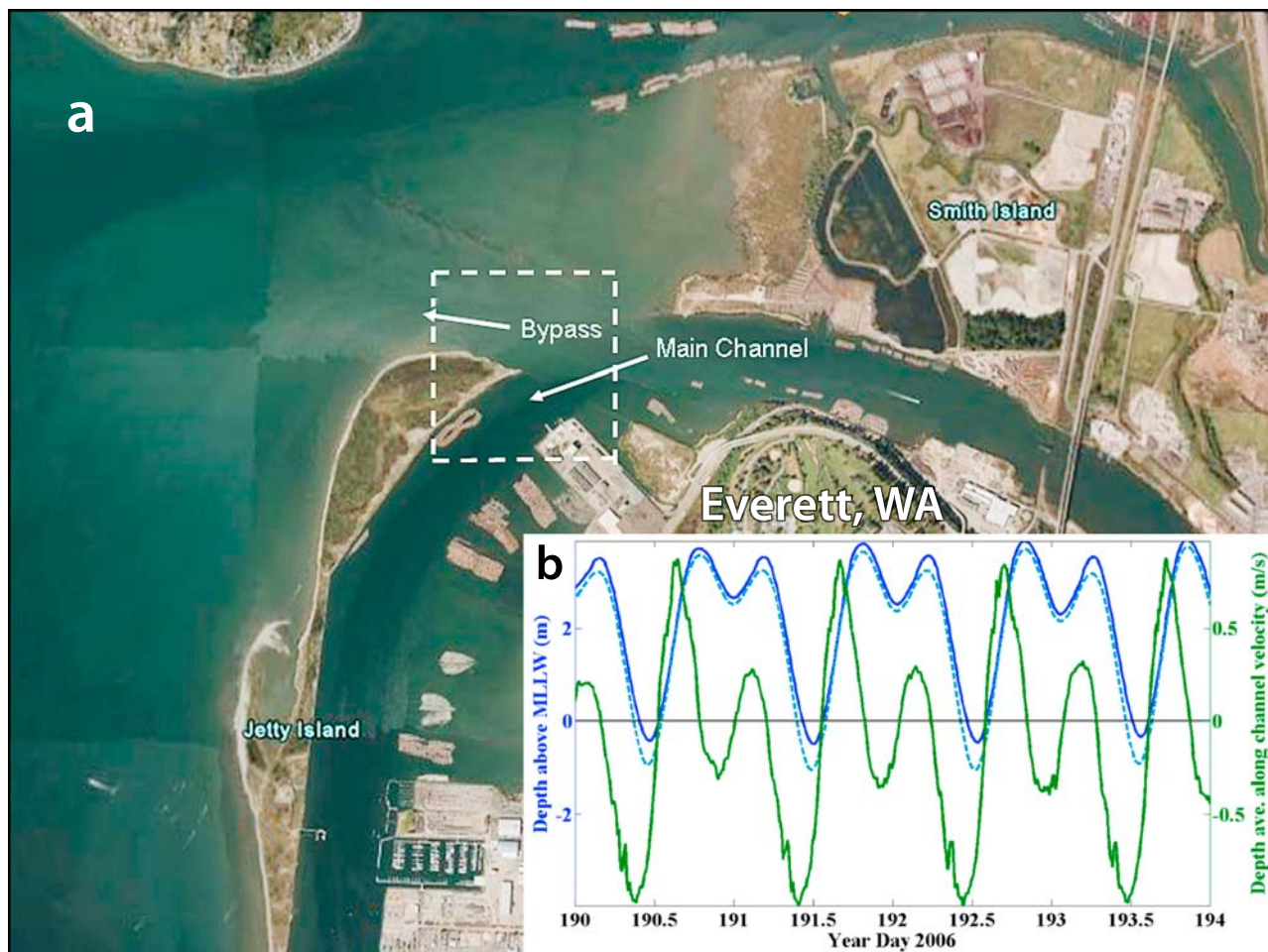
Figure 1. (a) Aerial photo of the location of the experiments on the Snohomish River at Everett, Washington. The dashed lines indicate the area addressed in most of the subsequent figures. North is up. The main channel of the river bends from west to south past the east side of Jetty Island, while a bypass goes along the north side of the island where mudflats exist at low tide. Google Earth imagery © Google Inc. Used with permission. (b) Tidal heights (blue) and measured currents (green) at the measurement site shown in the dashed lines. Solid blue lines are NOAA measurements in Seattle, and dashed blue lines are values measured at our site. Positive currents are upstream. Year day 190.5 is noon on 10 July.

current profiler (ADCP). All times used in this paper are Pacific daylight time.

2. Experiments

2.1. Experiment Site

[4] The experiments were conducted in the summers of 2005, 2006, and 2007 near the mouth of the Snohomish River at Everett, Washington, United States. Few radar images were produced in 2006 because of technical difficulties, and these will not be discussed here. Useable radar data were collected continuously from 18–27 July 2005 and from 2 August to 13 September 2007. Airborne optical and infrared data were collected for a total of 30 h between 7 and 20 July 2006. An aerial photo of the field site is shown in Figure 1a. In this region, the river flows past an artificial island, Jetty Island, into Puget Sound and is highly influenced by the tidal cycle acting as a salt wedge estuary. Figure 1b shows the relationship between water level (tidal height) and velocity in the system, which exhibits a strong

diurnal inequality. The tides are nearly standing waves with a slightly progressive nature, resulting in slack tide occurring about 50 min after low water and flood tide persisting until just after high water. Although the data presented in Figure 1 are from 2006, river flows in 2005 and 2007 were very similar, and thus, the water level and velocity phasing should be similar. Figure 1 includes in situ measurements of velocity and water level as well as measurements of water level from the National Oceanic and Atmospheric Administration (NOAA) tide gauge in Seattle while Figures 5, 9, 10, 11, 13, 14, 18, 19, and 20 only include water level as measured by the NOAA gauge. On the ebb tide, fresh water flows from the river into Puget Sound both along the main channel of the river and through an intertidal mudflat bypass along the north side of Jetty Island. At lower low water, a sill stretching southeast from the northeastern tip of Jetty Island is exposed; it is separated from the tip of Jetty Island by a narrow stream of water about 2 m deep. At this time, much of the mudflats are also exposed and the bypass is disconnected from Puget Sound, trapping middensity water
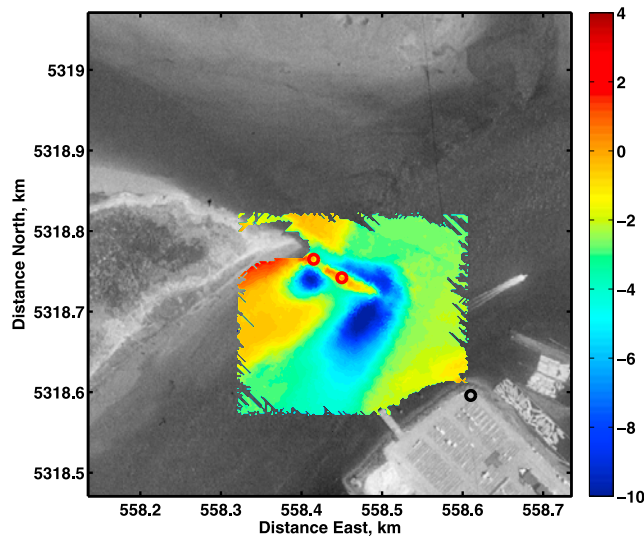
Figure 2. Bathymetry around the sill east of Jetty Island; the coordinate system is universal time meridian. The bathymetry was measured using a fathometer on a small boat in 2005 and is superimposed on an airborne optical (GeoTIFF) image of the area obtained in 1990 by the USGS as part of the National Aerial Photography Program. The color bar shows depth relative to mean low low-water level. The black circle at (558.61, 5318.6) km is the location of the Doppler radar called RiverRad; red circles show the locations of radar reflectors. The maximum extent of this image is the dashed white lines in Figure 1.

over the mudflats. During the ensuing large flood tide, dense Puget Sound water flowing back into the main channel converges with this middensity water from the mudflats, forming a front at their confluence (S. N. Giddings et al., Mixing and circulation in a shallow, macrotidal, saltwedge estuary, manuscript in preparation, 2009). The water from the mudflat region is much warmer than the river water because of a heat flux from the mud to the water. The mud is heated by the Sun before the tide comes in and through the shallow water after the tide comes in.

[5] In 2005, we measured the bathymetry around the sill using a fathometer in a small boat (Figure 2). At mean low low water, the highest point of the sill is about 1 m above the water surface, and it is roughly 50 m long by 6 m wide. A depression of the bed exists around the sill that has local minima where water flows through the gap between Jetty Island and the sill and just to the south of the eastern tip of the sill. The bed is deepest in the hole south of the tip of the sill, where it reaches a depth of about 10 m below mean low low water compared to a channel depth of about 2 m. The size of this hole is about 50 m in the southeast direction and 100 m in the southwest direction at 5-m depths.

[6] As part of these experiments, radar reflectors were mounted at locations on the tip of Jetty Island and on the sill. Their locations are denoted in Figure 2 by the red circles. Their universal time meridian coordinates in kilometers are (558.415, 5318.765) and (558.450, 5318.742). These radar reflectors are the red triangles mounted on the poles in Figure 3. Figure 3 also gives a good indication of the height of the sill at low tide and the extent of the gap

between the tip of Jetty Island and the sill; for scale, the far reflector pole is 3.1 m high.

2.2. Radar

[7] In all 3 years, RiverRad, a pulsed Doppler X band (9.36 GHz) radar built by the Applied Physics Laboratory of the University of Washington, was operated from a site across the river from the tip of Jetty Island. The location of the site is shown by the black circle in Figure 2 and the white dot (which is really a RiverRad antenna) in Figure 3. RiverRad is shown in operation at this site in Figure 4.

[8] Each antenna of RiverRad both transmitted and received. On straight sections of rivers, RiverRad can measure along- and cross-channel surface velocities using the Doppler shifts induced in signals scattered off the rough surface to antennas that are directed upstream and downstream [*Plant et al.*, 2005a; *Costa et al.*, 2006]. The river at this site was not straight, however, so in this paper we only present radial velocities, that is, the components of velocity along the antenna's line of sight. They are defined as positive toward the antenna. RiverRad also measures calibrated normalized radar cross sections of the backscattered power; these are always the cross sections displayed in this paper. Because it is pulsed, RiverRad measures cross sections and surface velocities in a variety of bins spaced equally in range.

[9] In these experiments, we always operated RiverRad at its highest range resolution, 3.75 m. The grazing angles of the antennas were about 1° below horizontal. The antennas were stepped through a series of azimuth angles 2° apart, holding each direction for approximately 1 min. Twenty such steps were made for a total swath width of about 40° for each antenna in about 20 min. This allowed us to create images of the tip of Jetty Island, part of the bypass, the sill, and the area between the sill and the radar. These 20-min sweeps alternated between clockwise and counterclockwise and were made sequentially over long periods of time. This characteristic of the radar operation allowed us to observe
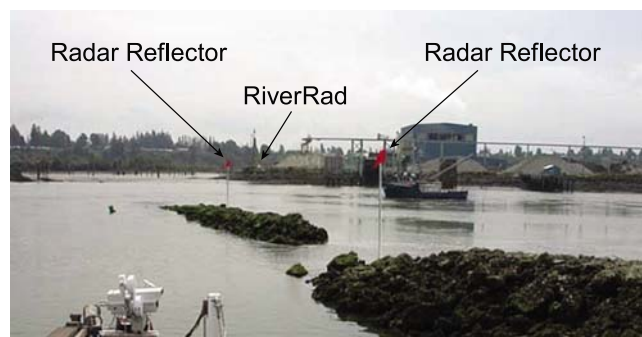

Figure 3. Two red radar reflectors mounted on poles. The near reflector is on the tip of Jetty Island, while the far one is in the center of the sill. The far reflector is 3.1 m above the sill. RiverRad is the white dot (in actuality, the antennas of RiverRad) just visible to the right of the far reflector about one fifth of the distance between the reflectors. This photograph was taken near the northeastern tip of Jetty Island looking eastward. The instrumentation in the bottom left corner is on a barge used for other measurements during the experiments.

Figure 4. RiverRad, a pulsed Doppler X band radar built by the Applied Physics Laboratory, University of Washington, shown in operation on the bank of the Snohomish River at Everett, Washington. Its location is indicated by the black circle in Figure 2 at (558.61, 5318.6) km.

repeated occurrences of the features reported here at particular phases of the tide.

[10] RiverRad's two parabolic antennas were set to look 36.6° apart in azimuth. In 2005, both antennas were operated with vertical polarization on both transmission and reception (VV). In 2007, the right antenna, that is, the one pointing toward higher azimuth (compass) angles, was changed to horizontal polarization on both transmission and reception (HH) polarization.

2.3. Infrared and Visible Airborne Instruments

[11] Infrared and visible frequency cameras were flown on a DHC-6-300 Twin Otter airplane over the river in July of 2006. The infrared imager was an AIM model 640Q long-wave instrument sensitive to radiation in the $8-10$ μm wavelength range. Both cameras viewed the water at nadir through an open camera port. The infrared imager was rotated up into the plane to view a blackbody for calibration to absolute temperature and nonuniformity correction. Imagery was later rectified to real-world coordinates on the basis of features identified in the images [Holland et al., 1997].

2.4. In Situ Measurements

[12] In situ hydrodynamic instrumentation mounted on moorings and transecting boats in 2005 and 2006 provided both spatial and temporal current and density measurements. During 2005 a transect loop, including transects both downstream and upstream of the sill and across the mudflat-river confluence, was repeated every 20 min with a boat-mounted 1200-kHz ADCP. The ADCP was operated in a high ping resolution mode at 1 Hz, measuring currents in 0.25-m-depth bins throughout the water column and allowing for approximately 1 m horizontal spatial resolution while transecting, which was subsequently averaged to 5-m horizontal bins. The shallowest bin of the ADCP-measured velocities was approximately 1 m beneath the water surface, allowing for a reasonable comparison with surface velocities computed from the radar. The ADCP velocity data were

recorded in beam coordinates and were rotated to coordinates aligned with the radial and cross-radial directions of the radar for comparison.

2.5. Numerical Model

[13] A high-resolution numerical model has been developed using the Stanford Unstructured Nonhydrostatic Terrain-Following Adaptive Navier-Stokes Simulator (SUNTANS) solver [Fringer et al., 2006] to study the flow around the sill at different stages of the tide. The model is a numerical model developed for the Snohomish River estuary using SUNTANS. Model setup and validation are described by Wang et al. [2009], and the results presented here follow exactly the same implementation except that the horizontal resolution around the sill has been significantly refined: (1) the computational mesh is refined to roughly 1 m; and (2) a 4-m bathymetric data set around the sill is employed, which is the best bathymetry currently available. With this resolution, the model should be able to capture the major spatial variability in the flow surrounding the sill. It is worth mentioning that validation of the model by Wang et al. [2009] was primarily based upon depth-averaged velocities. The surface velocity being compared to the radar data in this work could be less accurate because of errors in vertical mixing predicted by the turbulence closure used by the model.

3. Observed Surface Features

3.1. The Front

[14] RiverRad images of the monitored area at flood tide when the front existed between the main channel and the mudflat bypass are shown in Figure 5. Figure 5c shows a
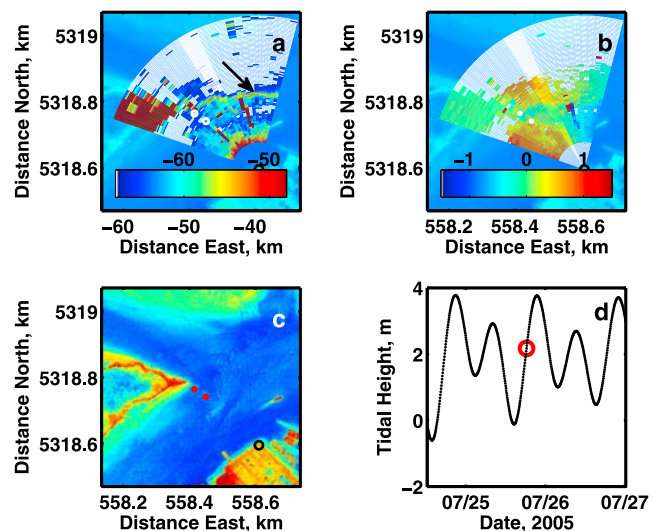

Figure 5. Imagery around the tip of Jetty Island on flood tide: (a) RiverRad normalized radar cross sections in dB and (b) RiverRad radial surface velocities in m/s (positive toward the radar) superimposed on the USGS GeoTIFF optical image of Figure 2. (c) The GeoTIFF image shown alone and color coded. (d) Time series of tidal height measured by NOAA in Seattle with the time of the images marked by the red circle. The arrow in Figure 5a points to the intense backscatter caused by the front, which is yellow in this image.
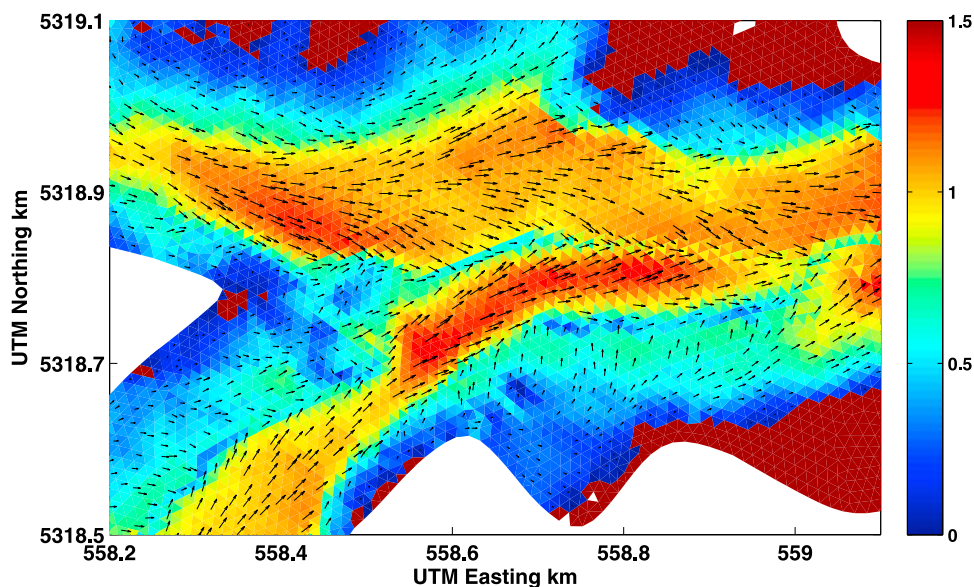
Figure 6. Surface velocities in m/s produced by the Stanford University numerical model near the confluence of bypass and main channel flow. The simulation is near the peak flood tide using the methods described by *Wang et al.* [2009].

color-coded version of the GeoTIFF optical image from Figure 2. RiverRad images are overlaid on this visible image in Figures 5a and 5b. Figure 5a presents RiverRad normalized radar cross sections in dB. If the received power was below the noise level of the radar, these could not be calculated. Such regions are shown in white in Figure 5a. Figure 5b shows radial surface velocities from RiverRad in m/s. These velocities cannot be measured if the cross sections are too low and are shown white in such regions. Finally, in Figure 5d, a time series of water level recorded at the NOAA gauge in Seattle is plotted, with the red circle indicating the time at which the radar images were taken. As demonstrated in Figure 1b, in situ measurements by Giddings et al. (manuscript in preparation, 2009) in 2006 indicated that water level at the field site does not vary significantly from that at the Seattle gauge.

[15] The imagery demonstrates that on the flood tide, a front forms between water from the bypass and that in the main channel. This phase of the tide is marked by a rising water level and the flow of Puget Sound water back into the Snohomish River. The front is marked by a line of intense radar backscatter in the cross-section image running from the tip of Jetty Island eastward (indicated by the arrows in Figure 1a). Radial surface velocities change abruptly at the front.

[16] The front was also observed in the velocity and density data obtained from the in situ transects and in the output of the numerical model. The surface velocities predicted by the model at flood tide are shown in Figure 6. They clearly show an east-west line of horizontal convergence near the location of the bright line in the radar cross-section image.

[17] We computed the component of these modeled surface velocities along the radar line of sight and compared them with the radial velocities measured by the radar. Figure 7 shows good qualitative correspondence between the convergent velocity fields. Additional direct compari-

sons with in situ instrumentation will be presented in an upcoming publication (S. N. Giddings et al., Comparative analysis of simultaneous in situ and remote sensing observations of a persistent front in a shallow macrotidal estuary, manuscript in preparation, 2009).

[18] Visible and infrared airborne imagery collected near the same tidal phase also showed this front. Examples are shown in Figure 8. The front's appearance in the visible image is due to surface roughness, but in the infrared imagery, the front is visible because of the temperature difference of warm water flowing back into the river from the mudflats and cool water from the main channel. Water flowing back into the river from the mudflats is warm because the mudflats are shallow and the water there has been heated by the mud and the Sun.

[19] Since the radar collected a long-term series of images, we were able to investigate the temporal evolution of this front in the radar imagery. We identified the line of high cross section in each image and picked five points along the line to plot as the location of the front. These points for various times on 25 July 2005 and on 14 August 2007 are shown in Figures 9 and 10, respectively. In 2005, the front seemed to be virtually stationary during the entire period of the measurements, except perhaps near the tip of Jetty Island, where it moved toward the south slightly as high tide was approached. In 2007, the front appeared to show far more movement toward the south as the water level approached its higher high water. This was a consistent difference for all measurements made in the 2 years.

3.2. Flow Over the Sill

[20] Another consistent difference between 2005 and 2007 in the radar imagery was the appearance of the roughness caused by flow over the sill near low tide. In 2005, this flow produced an intense area of higher radar cross section to the southwest of the sill as shown in Figure 11a. This implies higher surface roughness in this
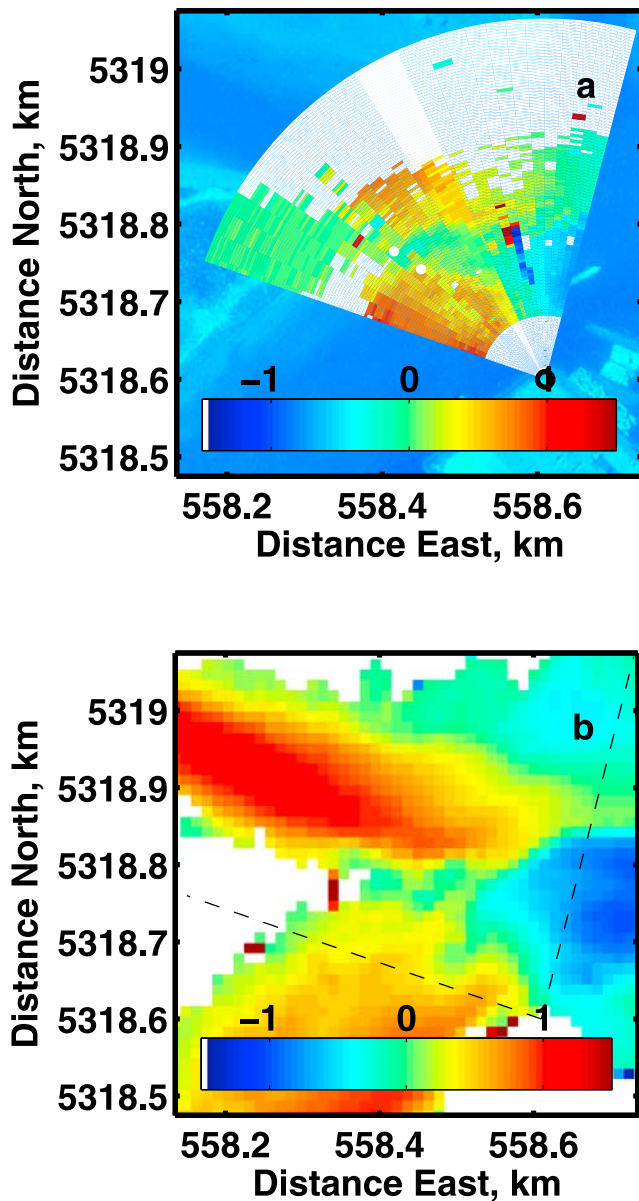
Figure 7. (a) Radial surface velocities from RiverRad overlaid on the GeoTIFF image. (b) Radial surface velocities from the Stanford University numerical model. Black dashed lines show the limits of the radar imagery. All velocities are in m/s, positive toward the radar.

the salt wedge. The water comes to the surface as boils which appear as cold circles in the infrared image and are surrounded by rough areas in the visible image [*Chickadel et al.*, 2009].

3.3. Flow Over the Hole

[22] Perhaps the most interesting of the remotely sensed river features was the surface expression of flow around the sill and over the hole south of the sill. In both 2005 and 2007, a set of nearly parallel bright lines appeared in the radar images to the southeast of the eastern tip of the sill near low tide. These lines were associated with mean radial surface velocities of about 0.5 m/s toward the radar anten-
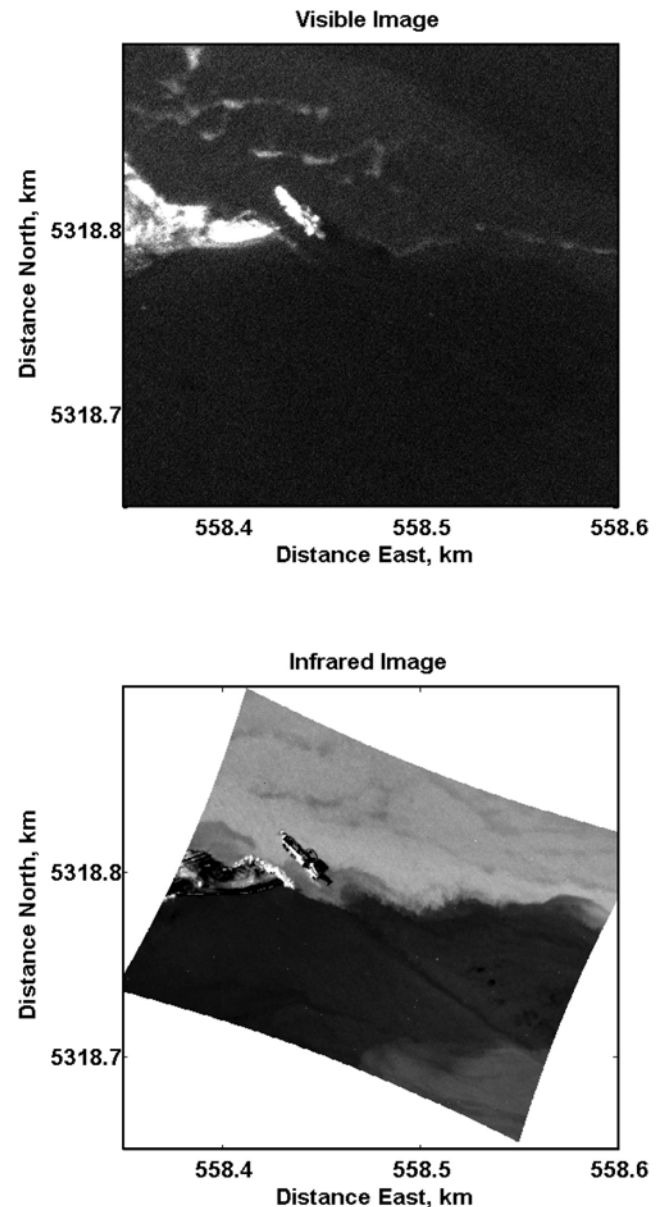

Figure 8. Coincident visible and infrared images collected by the airborne infrared and optical imagers flown on the Twin Otter at 1955 LT on 17 July 2006. Brighter areas represent warmer water in the infrared image. The barge used in other parts of these experiments is seen in the images just to the east of the tip of Jetty Island.
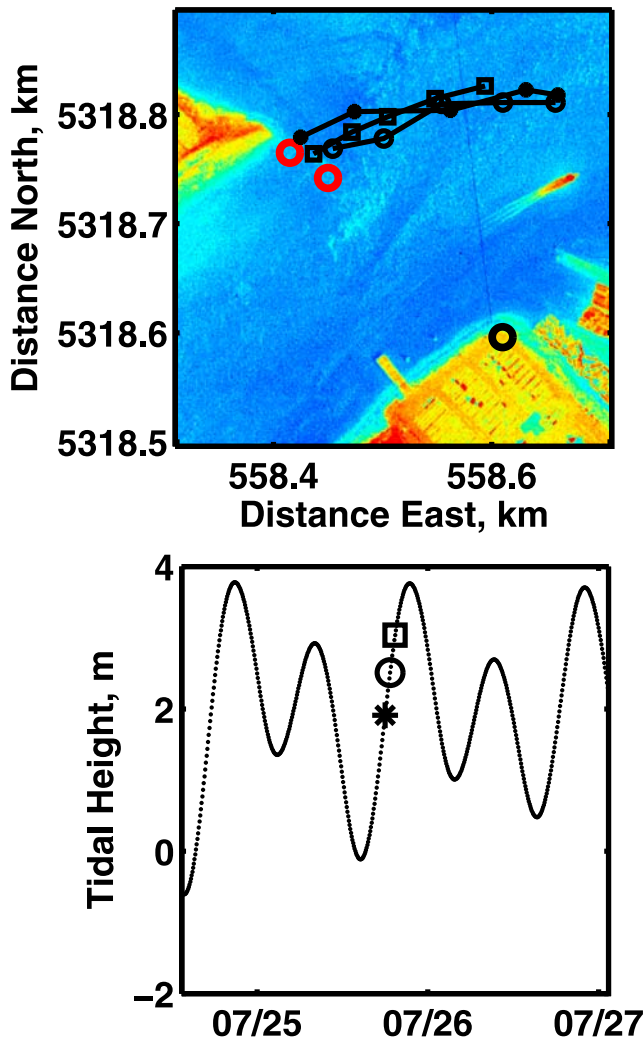
area caused by the turbulent flow over the sill. No mean radial surface velocities are associated with this turbulent flow, as shown in Figure 11b. In 2007, in contrast, this area of high return was seldom apparent. When it did appear, it was much weaker than in 2005.

[21] Visible and infrared airborne images collected in 2006 also showed surface expressions of the turbulence responsible for the high radar cross sections in the microwave images. Figure 12 gives examples of these images. The visible image shows the surface roughness features, while the infrared image shows that cold water is being brought to the surface southwest of the sill. The cold water originates from the presence of a dense bottom layer due to

Figure 9. (top) Locations of the front observed by RiverRad at selected times on 25 July 2005. Red circles indicate the radar reflectors. (bottom) Time series of tidal height with times of observation indicated by symbols matching those in Figure 9, top.

indicating colder water. For unstratified flow, this difference depends on the heat flux between the water and the air. A positive heat flux from the water causes the top layer of the water to be cooler than the bulk temperature, and the disturbed water will be warmer than surrounding water. When the heat flux is opposite, the disturbed water will be cooler than surrounding water [*Katsaros*, 1980]. If the water is stratified, as when returning Puget Sound water causes cold water to lie under warmer water, then boils can bring the cold water to the surface, resulting in dark signatures.

[24] Evidence that these image features are associated with the hole scoured into the bottom by flow around the end of the sill is shown in Figure 16. The radar cross-section image in Figure 16a clearly shows the two parallel bright lines. Figure 16b has white lines representing these parallel features overlaid on the optical image and bathymetry. The white lines are oriented in nearly the same direction as the sides of the hole and are located just slightly to the east of the deepest part of the hole.
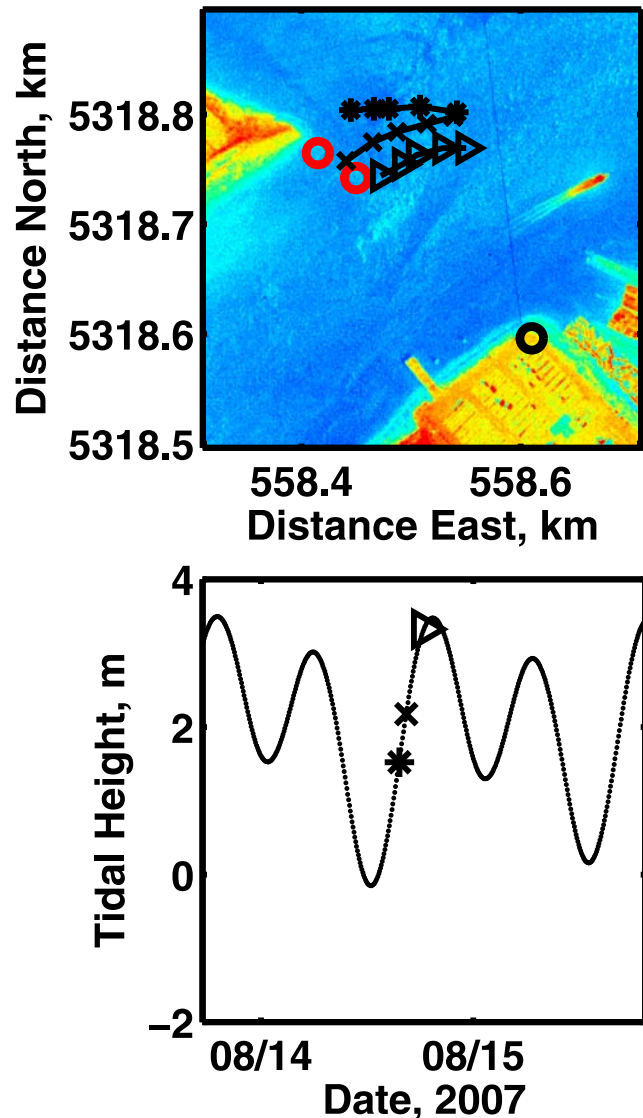
nas. This is documented in Figures 13 and 14. These lines were a rather consistent feature of the radar imagery around low tide in both years. Interestingly, the same features happen to show up in the GeoTIFF optical image that we have been using as a background map. In both Figures 13c and 14c, two parallel bright features appear in the precise location of those in the radar images.

[23] Effects of this flow over the hole can also be observed in the airborne visible and infrared imagery collected during 2006 (Figure 15). Note the two bright parallel lines in the visible image of Figure 15 and the signature of flow around the sill converging with the western line. These same features can be seen in the radar image shown in Figure 16a. The light-colored tongue indicating disturbed warm water to the southeast of the sill in the infrared image in Figure 15 covers the area between the two parallel lines seen in visible and microwave images. This signature is not always that of warm water. In other imagery, it appears as a dark area in the infrared image,

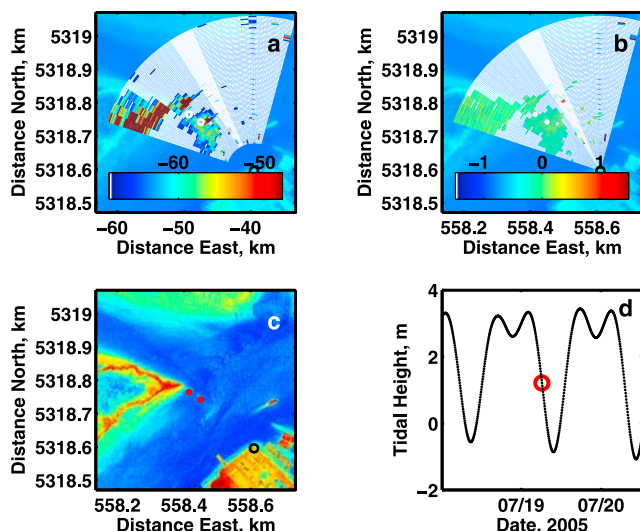**Figure 10.** Same as Figure 9 but on 14 August 2007.

Figure 11. (a) High radar cross sections and (b) low radial surface velocities observed by RiverRad just south of the sill in 2005 during an ebb tide. The higher cross sections imply higher turbulence downstream of the sill. (c) The standard color-coded GeoTIFF image and (d) time series of tidal height with the time of the images shown as a red circle. Red circles in Figures 11a and 11c show locations of the radar reflectors.

[25] Clearly, these features are produced when the tide is low by flow around the sill and over the abrupt change in bottom topography associated with the hole. Radar observations along the narrow axis of the hole are compared with ADCP current measurements and with model predictions along similar transects in Figure 17. The data shown in Figure 17b were obtained along the lines of the same color shown overlaid on a radar cross-section image in Figure 17a. Near-surface ADCP measurements are black, while model results are green; solid curves are radial velocities, and dashed ones are cross radial (azimuthal). Radial velocities deduced from radar Doppler spectra are shown as red lines for comparison. The dashed red line connecting open circles shows the range dependence of the normalized radar cross section, σ_o. The peaks near 140 and 160 m are the surface signatures of the hole caused by the increased surface roughness.

[26] These peaks appear to be located close to two positions where the ADCP radial velocity begins to increase rapidly. Past observations of radar surface signatures of bottom features have been explained on the basis of the modulation of short surface waves by current gradients associated with flow over the bottom topography [*Alpers and Hennings*, 1984]. This work indicated that only gradients in the component of current in the antenna look direction, radial velocities, cause the changes in cross section. This would be consistent with the observed peaks being caused by the increasing radial currents measured near them. However, this theory would require extremely large relaxation times for these short waves in order to explain the magnitudes (about 10 dB) of the cross-section changes observed here. Also, the further increase of the ADCP radial current near 180 m seems to cause no cross-section peak.

[27] Nevertheless, it is very likely that near-surface current gradients are the cause of the cross-section peaks, whether or not they are precisely explained by the theory of *Alpers and Hennings* [1984]. Such current gradients, for instance, explain the microwave surface expressions of both internal waves and long surface waves [*Keller and Wright*, 1975; *Alpers*, 1985; *Thompson and Gasparovic*, 1986]. However, the peak near 160 m in Figure 17b could also be associated with the increase of the gradient of azimuthal (cross-radial) current observed by the ADCP and predicted in nearly the same location by the model. A careful reading of the work by Alpers and Hennings shows that their
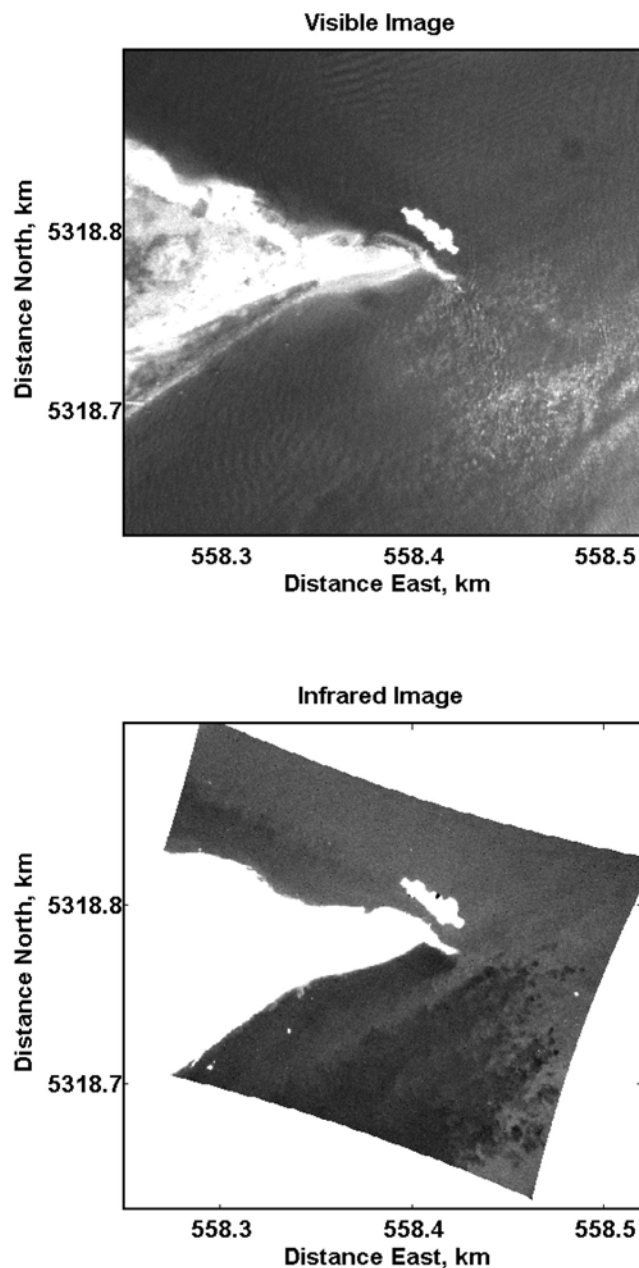

Figure 12. Coincident visible and infrared images collected from the airplane near midtide at 1041 LT on 14 July 2006. Darker areas represent colder water in the infrared image.
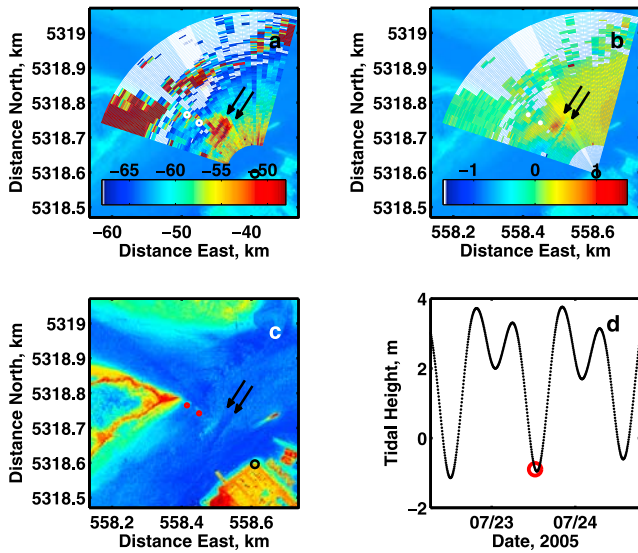
Figure 13. Parallel lines imaged in 2005 just to the southeast of the tip of the sill near low low water: (a) normalized radar cross sections in dB, (b) radial surface velocities in m/s, positive toward the radar, and (c) GeoTIFF image. The lines are associated with radial velocities toward the antennas (Figure 13b). (d) Time series of NOAA tidal heights with the times of the imagery indicated by the red circle. In Figures 13a, 13b, and 13c, the arrows point to the two parallel lines.

conclusion that only gradients of radial velocity cause cross-section change is really an assumption of their calculations (see their equation (29)). We believe that it is also possible that the cross-section peak near 160 m in Figure 17b is a result of the large change in cross-radial velocity or a combination of this gradient and that of the radial velocity.

4. Feature Visibility

[28] The existence or absence of surface features in radar data associated with the front, the sill, and the hole were
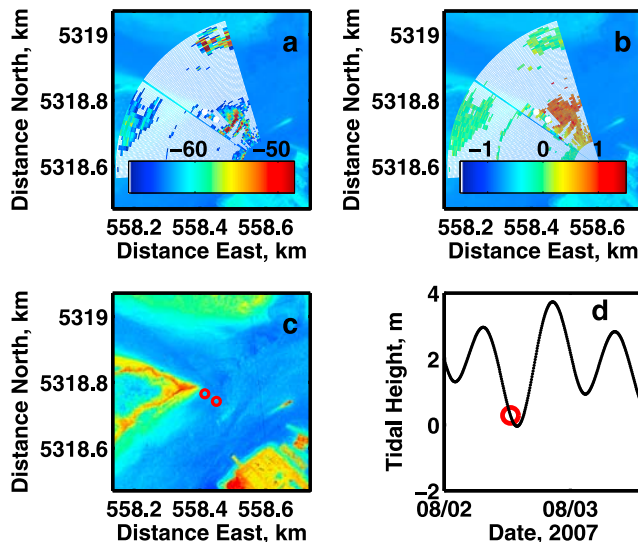

Figure 14. Same as Figure 13 but for 2007.

compared with tidal range, tidal phase, wind velocity, and river outflow. Wind velocities were obtained from NOAA measurements at Seattle, Washington, while river height was obtained from the U.S. Geological Survey (USGS) gauge at Snohomish, Washington. A synthesis of this analysis is presented in Figures 18 and 19.

[29] This synthesis suggests that in this case, river height, or stage, upstream is not the factor determining the visibility of the features since it is virtually constant over the course of the measurements. Wind direction is mostly from the western two quadrants and shows no clear correlation with feature visibility. Most of the features appear to be more
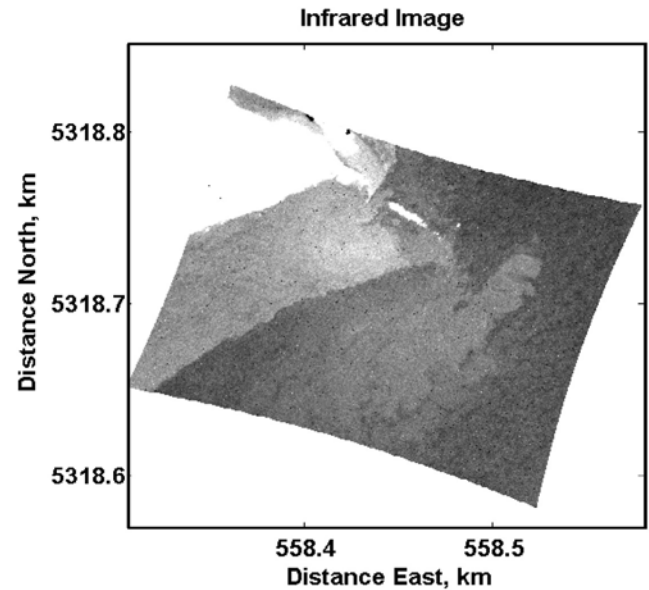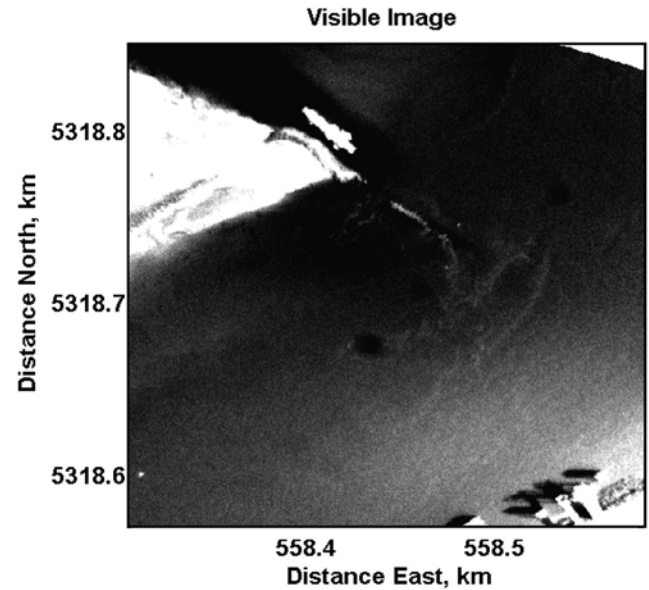

Figure 15. Coincident visible and infrared images collected from the airplane near low tide at 0831 LT on 9 July 2006. Brighter areas represent warmer water in the infrared image.
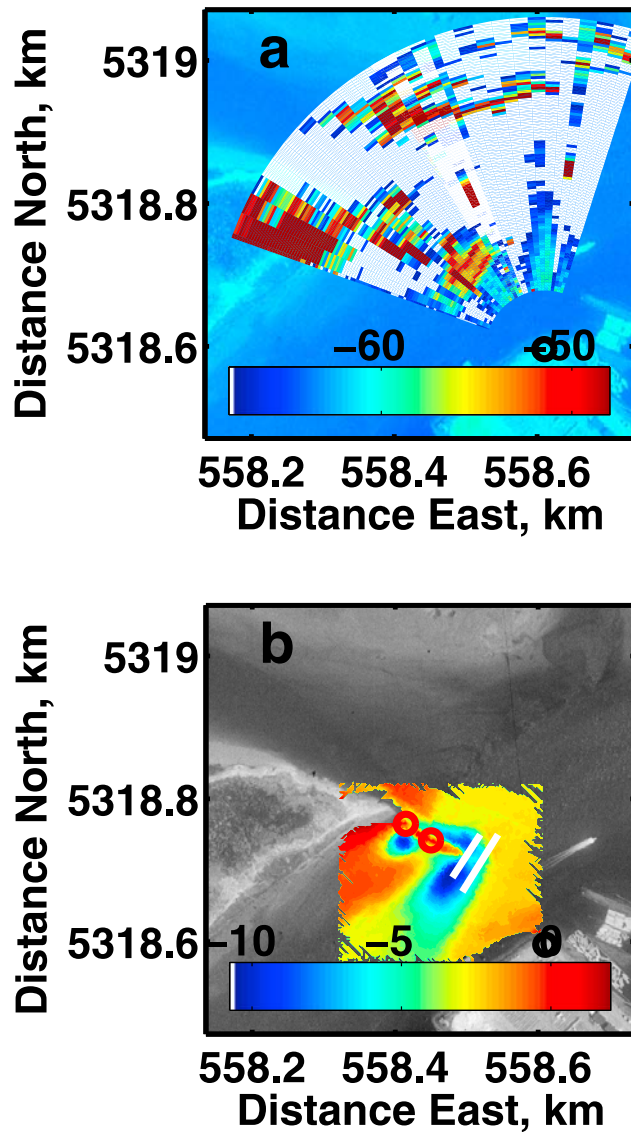
Figure 16. Coincidence between the image features observed near low tide and the sides of the hole near the southern tip of the sill. (a) The parallel lines of high radar cross section appear in red near (558.5, 5317.7). The large cross sections at distances above 5318.85 km are due to the exposed mudflats. (b) The white lines show the locations of the parallel lines with respect to bathymetric contours.

the surface. The surface signature of the sill is also far more apparent in the 2005 data than in the 2007 data. Finally, the parallel lines near the edges of the scour hole were always visible near lower low water that was at or below −1 m in 2005, a condition that did not occur in 2007. In both years, this feature only appeared when the water level dropped below the height of the sill (the red dashed lines in Figures 18 and 19), but it did not always appear under those conditions. It is interesting to note that unlike the front and the hole features which only appear on the largest floods and ebbs, respectively, the sill feature occurs on both large and small ebbs approaching low water.
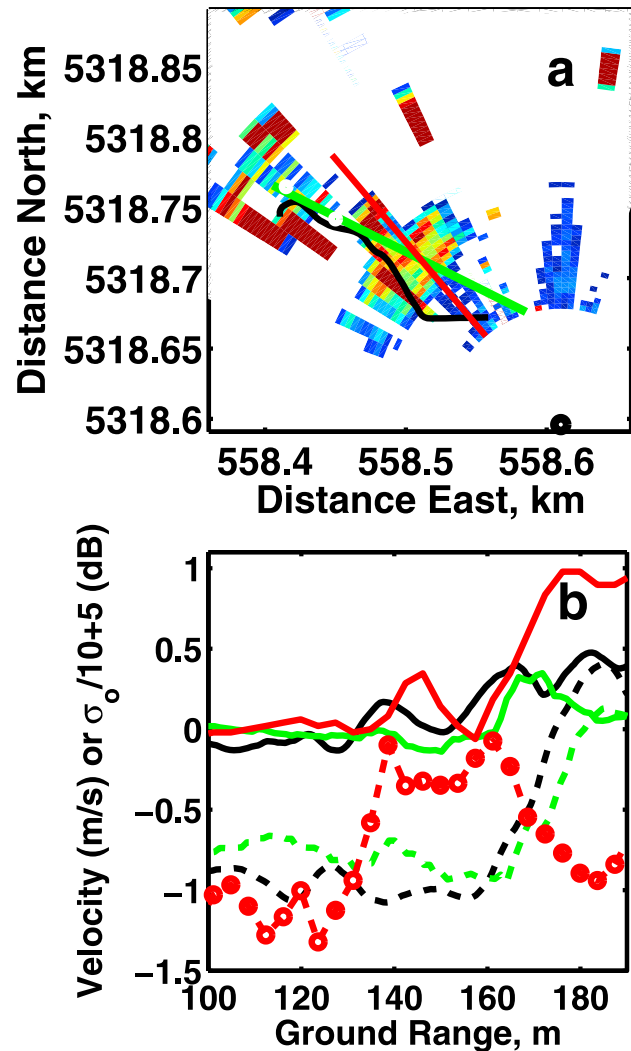

Figure 17. (a) The lines of high radar cross section shown along with the locations of the model predictions (green line), in situ ADCP data (black curve), and radar data (red line). (b) Data from the model, ADCP, and radar. Solid lines are radial velocities, positive toward the radar. Dashed lines are azimuthal (cross-radial) velocities, positive upstream (toward the top right corner in Figure 17a). The dashed line connecting open circles shows the radar cross section (in dB divided by 10 and with 5 added). Red always indicates radar data, black indicates ADCP data, and green indicates model predictions.

visible in 2005 than in 2007, and the wind speeds may differ somewhat in the two years. However, a clear dependence of feature visibility on tidal phase and tidal range is seen in both Figures 18 and 19. The frontal feature generally appears during flood tides after lower low water. This phase of the tide corresponds to maximum flood currents (Figure 1a), and the front often persists until slack tide near high water. However, the frontal surface expression does not always show up under these conditions. Similarly, the surface expression of the sill appears during the ebb tide well before the sill is exposed but seems to require the large ebb currents associated with a relatively low tidal minimum. If lower low water is not very low, the currents over the sill are weak at ebb tide, leading to weaker or no turbulence at
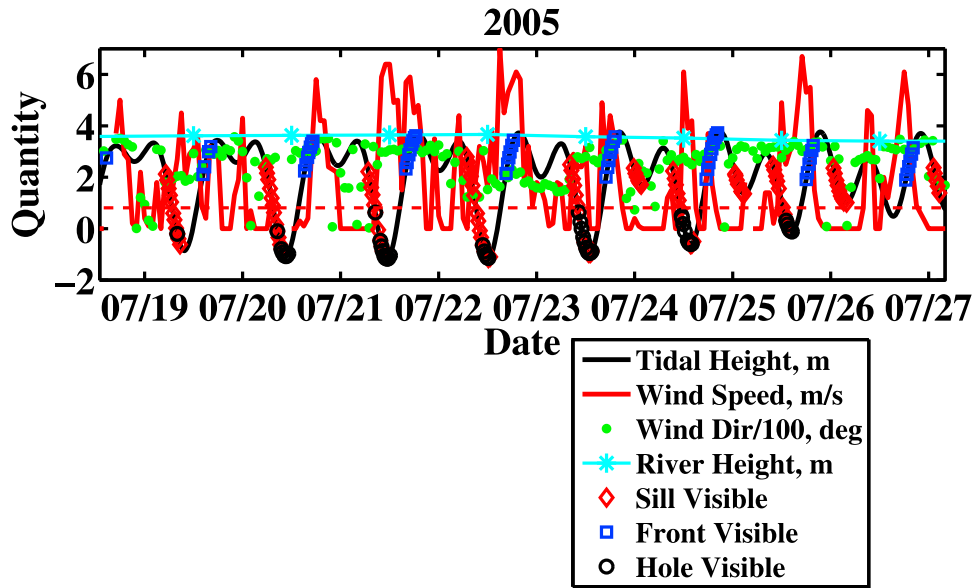
Figure 18. Times when the surface features were visible in the radar imagery of 2005. NOAA tidal height, wind speed and direction, and river height are also shown. The dashed red line is the maximum height of the sill.

[30] In 2005 the surface features were observed with VV polarization, while in 2007 they were all observed by the right antenna, which operated at HH polarization. Thus, radar polarization might account for the different feature visibility in the 2 years. This seems unlikely, however, since surface features are usually more prominent at HH than at VV [*Churyumov et al.*, 2002]. We therefore discount the polarization difference as a reason for the different feature visibility in the 2 years.

[31] Two other possibilities to explain the intermittent appearance of the features are wind speed and tidal range.

We examine these two possibilities by plotting various quantities associated with the radar images against the total tidal range between adjacent extrema in Figure 20. Figures 20a and 20b show the number of observations of the various features as a function of the change in tidal elevation (positive for rising tide) in 2005 and 2007, respectively. Recall from Figure 1b that the rising and falling tides roughly correspond to flood and ebb currents. As already noted, the front appears as the tide increases; the few observations of this feature in 2007 during decreasing tides are just after higher high water, likely when the
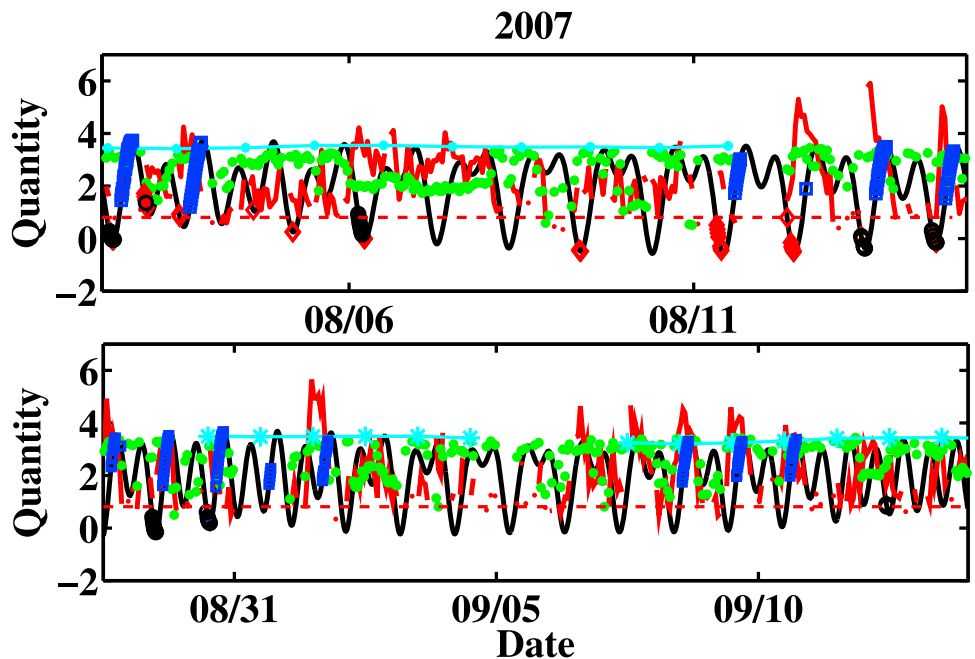

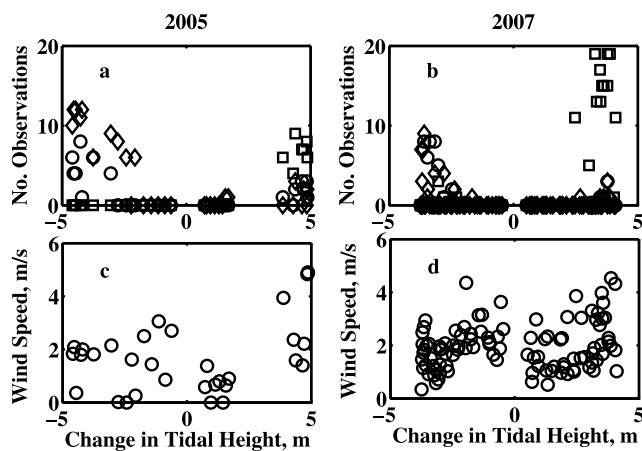**Figure 19.** Same as Figure 18 but for 2007.

Figure 20. Number of surface feature observations and mean wind speed plotted against the total change in tidal height (the tidal range) between extremes: (a) number of features in 2005, (b) number of features in 2007, (c) wind speed in 2005, and (d) wind speed in 2007. The change in tidal height is a proxy for current magnitudes. In Figures 20a and 20b, squares indicate that the frontal feature was visible, diamonds indicate that the sill feature was visible, and circles indicate that the parallel lines beside the hole were visible.

currents are still very weakly flooding. The sill and hole surface features appear during falling tides and near low water. One obvious feature of Figure 20b is that no tidal ranges greater than 4.1 m in magnitude occurred in 2007. The region with tidal ranges above about 4 m in magnitude was where most of the features appeared in 2005. Thus, the visibility of the features requires the high currents associated with a large tidal range. Nevertheless, the plots show times when the magnitude of the tidal range is large but no features appear. Therefore, a large tidal range and the associated high currents appear to be a necessary but not sufficient condition for the features to appear.

[32] Figures 20c and 20d document the mean wind speeds for 2005 and 2007, respectively, for various tidal ranges. As one would expect, no correlation is seen between these two variables, but the wind speeds appear to be marginally higher in 2007 than in 2005. However, most mean wind speeds over periods of tidal change are less than 2.3 m/s. This is the threshold for wind generation of the short waves that scatter microwaves when no currents are present [*Donelan and Pierson*, 1987; *Plant*, 2000; *Donelan and Plant*, 2009]. This threshold changes with surface currents, dropping for currents opposite the wind and increasing when they are parallel. However, the threshold will be higher for waves not propagating exactly in the wind direction. Since the radar only views short waves traveling in its look direction, these waves are seldom traveling in the wind direction. Therefore, the observed features appear to be primarily due to roughness on the surface of the river generated by the phenomena themselves rather than by the modulation of wind-generated waves. This conclusion is supported by the observation that maximum normalized radar cross sections of all the features observed here are less than −50 dB, while the minimum cross section for steady wind-generated waves of the same Bragg wavelength at this

incidence angle is well above this value [*Donelan and Plant*, 2009; *Plant*, 1990]. Current gradients can cause either type of roughness variations, but stronger gradients are required to generate the roughness than to modulate existing wind-driven roughness. We tentatively conclude that small current gradients are the reason that features sometimes do not appear even when tidal ranges are large.

5. Conclusion

[33] We have shown that images of river surfaces obtained in microwave, infrared, and visible frequency ranges contain features related to the flow driven by complex bathymetry. The images were collected on the Snohomish River near its mouth at Everett, Washington. The observed surface features were produced by a front that occurred at the convergence of two different density water masses during flood tide, a sill on the bottom that was observed in the imagery before it was exposed at low tide and a scour hole that existed south of the sill and was observed in imagery near lower low water. Our modeling and in situ measurements show that the front and the hole both generate near-surface current gradients that cause the observed microwave and visible features. Features in the infrared images are somewhat harder to model or relate to in situ measurements because they are related to the advection of deep water to the surface by boils. Progress on this front, however, is being made [*Chickadel et al.*, 2009].

[34] Our work shows that the front at the confluence of water flowing through the bypass around Jetty Island and that flowing through the main channel at flood tide is sometimes nearly stationary and sometimes moves to the south as high tide is approached. The sill effects are visible in the flow when the sill is submerged by more than 2 m, while the surface effects due to the hole can be detected at times just as the sill becomes exposed. All of these features appear only when tidal ranges are large, corresponding to relatively high velocities. However, they are not always observed under these conditions.

[35] The low winds that occurred during our experiments imply that the roughness that allows the features to be observed by microwave radars and visible imagers is usually generated not by the wind but by properties of the flow itself. In the cases of the front and the hole, in situ observations and the numerical model suggest that this property is probably the horizontal shear in the surface currents generated by the features. In the case of flow over the sill, the roughness is probably caused by the turbulence generated at the surface by flow over the sill, which is observed by both in situ instrumentation and infrared imagery.

[36] This work demonstrates that remotely sensed data from rivers and estuaries can be used to constrain models. Surface features observed remotely must be reproduced in model output. In the modeling work presented here, current gradients responsible for the surface visibility of the hole did not appear in model results until sufficiently high resolution bathymetry was used. Thus, the remote sensing data contributed to improved modeling of bottom features.

References

Alpers, W. (1985), Theory of radar imaging of internal waves, *Nature*, *314*, 245–247, doi:10.1038/314245a0.

Alpers, W., and I. Hennings (1984), A theory of the imaging mechanism of underwater bottom topography by real and synthetic aperture radar, *J. Geophys. Res.*, *89*, 10,529–10,546, doi:10.1029/JC089iC06p10529.

Bjerklie, D. M., D. Moller, L. C. Smith, and S. L. Dingman (2005), Estimating discharge in rivers using remotely sensed hydraulic information, *J. Hydrol.*, *309*, 191–209, doi:10.1016/j.jhydrol.2004.11.022.

Brakenridge, G. R., J. C. Knox, E. D. Paylor, and F. J. Magilligan (1994), Radar remote sensing aids study of the Great Flood of 1993, *Eos Trans. AGU*, *75*(45), 521.

Chickadel, C. C., A. R. Horner-Devine, S. A. Talke, and A. T. Jessup (2009), Vertical boil propagation from a submerged estuarine sill, *Geophys. Res. Lett.*, *36*, L10601, doi:10.1029/2009GL037278.

Churyumov, A. N., Y. A. Kravtsov, O. Y. Lavrova, K. T. Litovchenko, M. I. Mityagina, and K. D. Sabinin (2002), Signatures of resonant and non-resonant scattering mechanisms on radar images of internal waves, *Int. J. Remote Sens.*, *23*(20), 4341–4355, doi:10.1080/01431160110107644.

Costa, J. E., K. R. Spicer, R. T. Cheng, F. P. Haeni, N. B. Melcher, E. Michael, W. J. Plant, and W. C. Keller (2000), Measuring stream discharge by non-contact methods: A proof-of-concept experiment, *Geophys. Res. Lett.*, *27*, 553–556, doi:10.1029/1999GL006087.

Costa, J. E., R. T. Cheng, F. P. Haeni, N. Melcher, K. R. Spicer, E. Hayes, W. J. Plant, K. Hayes, C. Teague, and D. Barrick (2006), Use of radars to monitor stream discharge by noncontact methods, *Water Resour. Res.*, *42*, W07422, doi:10.1029/2005WR004430.

Donelan, M. A., and W. J. Pierson Jr. (1987), Radar scattering and equilibrium ranges in wind-generated waves with application to scatterometry, *J. Geophys. Res.*, *92*, 4971–5030, doi:10.1029/JC092iC05p04971.

Donelan, M. A., and W. J. Plant (2009), A threshold for wind-wave growth, *J. Geophys. Res.*, *114*, C07012, doi:10.1029/2008JC005238.

Fringer, O. B., M. Gerritsen, and R. L. Street (2006), An unstructured-grid, finite-volume, non-hydrostatic, parallel coastal ocean simulator, *Ocean Modell.*, *14*, 139–173, doi:10.1016/j.ocemod.2006.03.006.

Holland, K. T., R. A. Holman, T. C. Lippmann, J. Stanley, and N. Plant (1997), Practical use of video imagery in nearshore oceanographic field studies, *IEEE J. Oceanic Eng.*, *22*(1), 81–92, doi:10.1109/48.557542.

Horritt, M. S., D. C. Mason, and A. J. Luckman (2001), Flood boundary delineations from synthetic aperture radar imagery using a statistical active contour model, *Int. J. Remote Sens.*, *22*(13), 2489–2507, doi:10.1080/01431160152497691.

Katsaros, K. B. (1980), The aqueous thermal boundary layer, *Boundary Layer Meteorol.*, *18*, 107–127, doi:10.1007/BF00117914.

Keller, W. C., and J. W. Wright (1975), Microwave scattering and the straining of wind-generated waves, *Radio Sci.*, *10*(2), 139–147, doi:10.1029/RS010i002p00139.

Melcher, N. B., et al. (2002), River discharge measurements by using helicopter-mounted radar, *Geophys. Res. Lett.*, *29*(22), 2084, doi:10.1029/2002GL015525.

Plant, W. J. (1990), Bragg scattering of electromagnetic waves from the air/sea interface, in *Surface Waves and Fluxes*, vol. 2, *Remote Sensing*, edited by G. L. Geernaert and W. J. Plant, pp. 41–108, Kluwer Acad., Dordrecht, Netherlands.

Plant, W. J. (2000), Effects of wind variability on scatterometry at low wind speeds, *J. Geophys. Res.*, *105*, 16,899–16,910, doi:10.1029/2000JC900043.

Plant, W. J., W. C. Keller, and K. Hayes (2005a), Measurement of river surface currents with coherent microwave systems, *IEEE Trans. Geosci. Remote Sens.*, *43*, 1242–1257, doi:10.1109/TGRS.2005.845641.

Plant, W. J., W. C. Keller, K. Hayes, and K. R. Spicer (2005b), Streamflow properties from time series of surface velocity and stage, *J. Hydraul. Eng.*, *131*, 657–664, doi:10.1061/(ASCE)0733-9429(2005)131:8(657).

Romeiser, R., H. Runge, S. Suchandt, J. Sprenger, H. Weilbeer, A. Sohrmann, and D. Stammer (2007), Current measurements in rivers by space-borne along-track InSAR, *IEEE Trans. Geosci. Remote Sens.*, *45*, 4019–4031, doi:10.1109/TGRS.2007.904837.

Spicer, K. R., J. E. Costa, and G. Placzek (1997), Measuring flood discharge in unstable stream channels using ground-penetrating radar, *Geology*, *25*, 423–426, doi:10.1130/0091-7613(1997)025<0423:MFDIUS>2.3. CO;2.

Thompson, D. R., and R. F. Gasparovic (1986), Intensity modulation in SAR images of internal waves, *Nature*, *320*, 345–348, doi:10.1038/320345a0.

Wang, B., O. B. Fringer, S. N. Giddings, and D. A. Fong (2009), High-resolution simulations of a macrotidal estuary using SUNTANS, *Ocean Modell.*, *26*, 60–85, doi:10.1016/j.ocemod.2008.08.006.

Yamaguchi, T., and K. Niizato (1994), Flood discharge measurement using radio current meter (in Japanese), *Pap. Jpn. Soc. Civ. Eng.*, *497*(II-28), 41–50.

———————————

R. Branch, G. Chatham, C. C. Chickadel, K. Hayes, A. Jessup, and W. J. Plant, Applied Physics Laboratory, University of Washington, 1013 NE 40th Street, Box 355640, Seattle, WA 98105, USA. (plant@apl.washington.edu)

O. B. Fringer, D. A. Fong, S. N. Giddings, S. Monismith, and B. Wang, Department of Civil and Environmental Engineering, 473 Via Ortega, Stanford University, Stanford, CA 94305, USA.

B. Hayworth, U. S. Environmental Protection Agency, 1595 Wynkoop Street (8P-W-TF), Denver, CO 80202, USA.

A. Horner-Devine, Department of Civil and Environmental Engineering, University of Washington, 201 More Hall, Box 352700, Seattle, WA 98195, USA.